Research Article | Vol. 27, No. 21 / 14 October 2019 / Optics Express 30055
Optics EXPRESS

Label-free CARS microscopy through a multimode fiber endoscope

JOHANNA TRÄGÅRDH,[1,5,*] TOMÁŠ PIKÁLEK,[1,5] MOJMÍR ŠERÝ,[1] TOBIAS MEYER,[2,3] JÜRGEN POPP,[2,3] AND TOMÁŠ ČIŽMÁR[1,2,4]

[1]*Institute of Scientific Instruments of the CAS, v. v. i., Královopolská 147, 612 64 Brno, Czech Republic*
[2]*Leibniz Institute of Photonic Technology, Albert-Einstein-Straße 9, 07745 Jena, Germany*
[3]*Institute of Physical Chemistry, Friedrich Schiller University of Jena and Abbe Center of Photonics, Helmholtzweg 4, 07743 Jena, Germany*
[4]*Institute of Applied Optics, Friedrich Schiller University Jena, Fröbelstieg 1, 07743 Jena, Germany*
[5]*These authors contributed equally to the work*
[*]*johanna@isibrno.cz*

Abstract: Multimode fibres have recently been employed as high-resolution ultra-thin endoscopes, capable of imaging biological structures deep inside tissue *in vivo*. Here, we extend this technique to label-free non-linear microscopy with chemical contrast using coherent anti-Stokes Raman scattering (CARS) through a multimode fibre endoscope, which opens up new avenues for instant and *in-situ* diagnosis of potentially malignant tissue. We use a commercial 125 µm diameter, 0.29 NA GRIN fibre, and wavefront shaping on an SLM is used to create foci that are scanned behind the fibre facet across the sample. The chemical selectivity is demonstrated by imaging 2 µm polystyrene and 2.5 µm PMMA beads with per pixel integration time as low as 1 ms for epi-detection.

1. Introduction

Scattering effects make biological tissues largely opaque to light, which prevents use of versatile and high resolution light microscopy at depth. On the other hand, non-invasive medical imaging approaches offering imaging at large depths such as MRI, CT or ultrasound, do not allow for sufficient resolution and specificity for tasks such as tumour diagnosis. As a result, in the majority of oncological diagnoses and treatments, extracting biopsy samples from abnormally appearing tissue and performing histopathology under a high-magnification microscope is the current gold-standard diagnosis procedure. The remote and time-consuming nature of the histopathology assessment delays decision making considerably, and requires multiple surgical procedures. To address these shortcomings, there is an urgent need to develop a high-resolution label-free imaging approach, giving instant diagnostic information, which could be applied at depth in living organisms without causing a substantial damage to the tissue.

Efforts have been made in developing label-free methods such as linear Raman microscopy, CARS and Stimulated Raman Scattering (SRS) [1,2] for cancer diagnosis also via endoscopic probes [3,4], which, unfortunately, are far from having a footprint that is tolerable for use at depth in tissue. However, results of intensive research in light propagation through complex and random media, as well as advances in wavefront-shaping methods to control the light propagation [5,6] have provided us with the tools to transform a simple multimode fibre into a laser-scanning microscope. By shaping the input wavefront, the speckle pattern normally associated with transport of coherent light through a multimode fibre is turned into a single diffraction-limited focus [7], which can be rapidly scanned across a three-dimensional volume at the fibre end. Such multimode fibre-based endoscopes have an ultra-narrow foot-print (~100 µm) and their numerical aperture (NA) can reach that of high-magnification objectives [8], thus offering imaging depths an order of magnitude larger than that of multiphoton microscopes [9] with comparable resolution.

#375673 https://doi.org/10.1364/OE.27.030055
Journal © 2019 Received 16 Aug 2019; revised 24 Sep 2019; accepted 25 Sep 2019; published 2 Oct 2019

Optics EXPRESS

This since the endoscope can be inserted deep into the tissue with minimal damage. This concept has already proved useful for *in vivo* fluorescence imaging of brain [10,11]. Furthermore, advanced imaging methods such as light sheet [12] and multi-photon imaging [13–15] have been demonstrated using a multimode fibre endoscope.

Adding label-free imaging with chemical contrast, such as CARS, to this toolbox would make such endoscopes highly suitable for the *in situ* diagnostic tasks discussed above. CARS is particularly suitable for diagnostic purposes that rely on differentiating key cell components such as lipids, protein and water, since only a few wavelengths of the Raman spectrum are required for this [1,2,16], making the method much faster than linear Raman imaging. Such linear Raman imaging through a multimode fibre endoscope was demonstrated in [17,18], with characteristically long integration times of a few seconds. CARS is also the current emerging standard for imaging lipid structures [19]. Imaging lipid structures and droplets is relevant to elucidate the mechanisms of a number of disease conditions such as diabetes, atherosclerosis, and neurodegenerative conditions resulting from demyelination of axons [20,21]. CARS can also assist with overcoming the issues with the lack of specific staining dyes which hampers the visualization of the formation, transport and destruction of lipid droplets in cells [22].

Here, we demonstrate for the first time CARS microscopy down an ultra-narrow multimode fibre-based endoscope. The instrument employs commercial graded-index (GRIN) fibre with NA of 0.29 and outer diameter 125 µm. Using wavefront-shaping at a single spatial light modulator (SLM) the pump and the Stokes pulses are overlapped in space and time and focused and scanned across the sample. We demonstrate that epi-detection is possible despite the small probe size and high forward directionality of the CARS signal. When imaging in tissue, the epi-detection relies entirely on back scattering by the tissue of the forward emitted signal [23] and is therefore critically dependent on the collection area [24].

This new tool can significantly enhance the capabilities for *in-vivo* imaging of lipid metabolism and biological structures and, if used as a component in multimodal imaging, instant, *in situ*, tumour diagnosis. Importantly, this study also opens up for other non-linear imaging methods down a fibre such as THG, which have similarly forward directed emission [25]. Furthermore, the technique inherently offers a desirable axial sectioning due to the non-linear dependence of the emission on the excitation intensity.

2. Methods

For multimode fibre-based techniques, the imaging is preceded by a calibration step, in which the light transport through the fibre is analysed [7,10]. Using this information, focal points, where the pump and the Stokes pulse are overlapped in time and space, can be created. Each focal position corresponds to a specific pattern on the SLM and by displaying a sequence of patterns on the SLM, the focus (containing both pulses) is scanned across a plane 50 µm from the output facet of the multimode fibre, mimicking a laser scanning microscope.

2.1. Fibre imaging setup

A schematic of the setup is shown in Fig. 1. A Ti:Sapphire laser emitting ps pulses (Mira HP, Coherent) centered at 830–832 nm was used to pump an OPO (APE, Berlin). Part of the Ti:Sapphire power was picked off using a beam splitter and used as the CARS Stokes beam, and the output from the OPO in the range 661–668 nm with a bandwidth of 0.5–0.9 nm was used as the CARS pump beam. The pump beam was sent via a delay stage to control the time overlap of the pump and Stokes pulses. The beams were overlapped on a dichroic mirror and then expanded to fill the spatial light modulator (SLM) using a pair of achromatic lenses. The SLM used for the data in Fig. 2(a)–2(c) (dataset 1) was a Meadowlark HSP512-1064, and for the data in Figs. 3 and 4 (dataset 2), a Meadowlark HSP1920-1064-HSP8. The SLM was used in an off-axis configuration. Two patterns were applied to the SLM: the pattern for creating the focused

Optics EXPRESS

spot at the fibre output, and a plain blazed grating, giving a reference beam for calibration. After passing through a lens (f = 250 mm), the phase modulated first-order reflections corresponding to the different patterns were separated in the back focal plane of the lens. The reference beam and the zeroth order beam were picked-off using a D-shaped mirror and the reference was isolated using an iris. For the remaining light, that was coupled to the multimode fibre, the fibre core acted as a filter to remove light from higher diffraction orders.

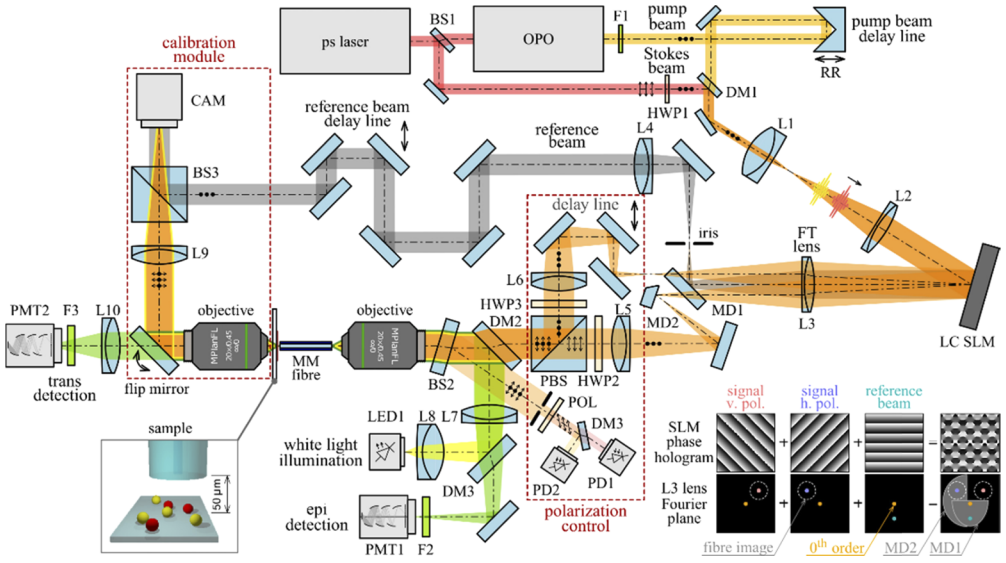

Fig. 1. Schematic of the setup for performing CARS imaging through the multimode fibre. DM = Dichroic mirror, MD = D-shaped mirror, L = lens, PBS = polarizing beam splitter, BS = beam splitter, MM fibre = multimode fibre, LC SLM = spatial light modulator, HWP = half wave plate, PD = photo detector, CAM = Camera, POL = polarizer, F = filter. The calibration module, indicated by a dashed box, can be removed after the calibration step to allow imaging of thick non-transparent samples [10]. The inset shows the method for controlling two polarizations and generating a reference beam on the same single SLM. The top row shows the patterns applied to the SLM and the bottom row shows the image of the Fourier plane of lens L3, where the beams corresponding to the different patterns are separated using MD1, MD2 and an iris.

In order to minimise the optical power in the speckle pattern around the focused spot in the imaging plane, which is inherent in imaging through multimode fibres, and thus maximise the power in the spot itself, the polarisation of the light coupled into the fibre had to be controlled [7]. This is particularly important for GRIN fibres, which completely scramble the polarisation of the input light [14], resulting in an equal intensity of light in the two distinctly different speckle patterns for the two orthogonal polarisations. The polarization control was achieved by combining two patterns on the SLM; one for each polarisation, and directing the beams to different positions in the Fourier plane of the SLM (see inset in Fig. 1). Each beam was then collimated using an f = 200 mm achromatic lens. The polarisation of one of the beams was rotated using an achromatic half wave plate. The other beam was passed through a half wave plate with its fast axis aligned with the polarisation to keep the dispersion in the two beam paths the same. These beams were re-combined on a polarising beam splitter, and their path length difference was adjusted to close to zero using a delay stage. The beams were focused on the multimode fibre facet using a 20X NA 0.45 objective lens. The SLM was imaged to the back-focal plane of the objective. The diameter of the beam at the back focal plane of the objective was chosen to

Optics EXPRESS

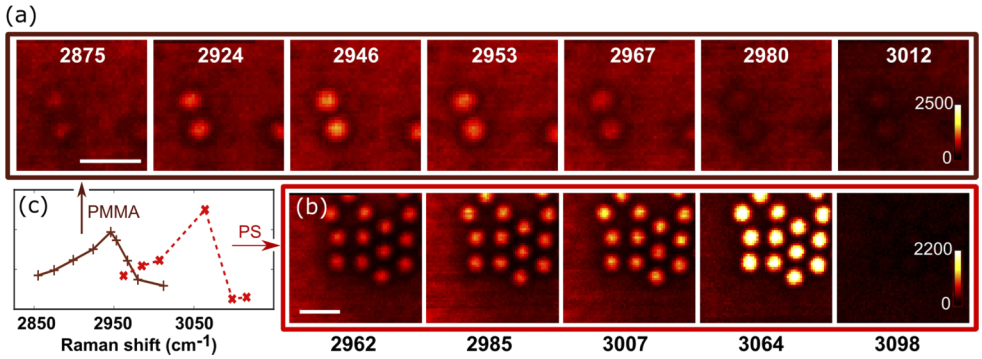

Fig. 2. CARS images of (a) 2.5 µm diameter PMMA and (b) 2 µm diameter PS beads detected in transmission. The frequency difference in cm^{-1} between the Stokes beam and the pump beam is indicated in each image. (c): The intensity of the CARS signal in (a) (brown crosses, solid line) and (b) (red crosses, dashed line) as a function of frequency difference between Stokes and pump beam. The lines are a guide to the eye. The images in (a) and (b) are a subset of the data presented in (c). Scalebars are 5 µm.

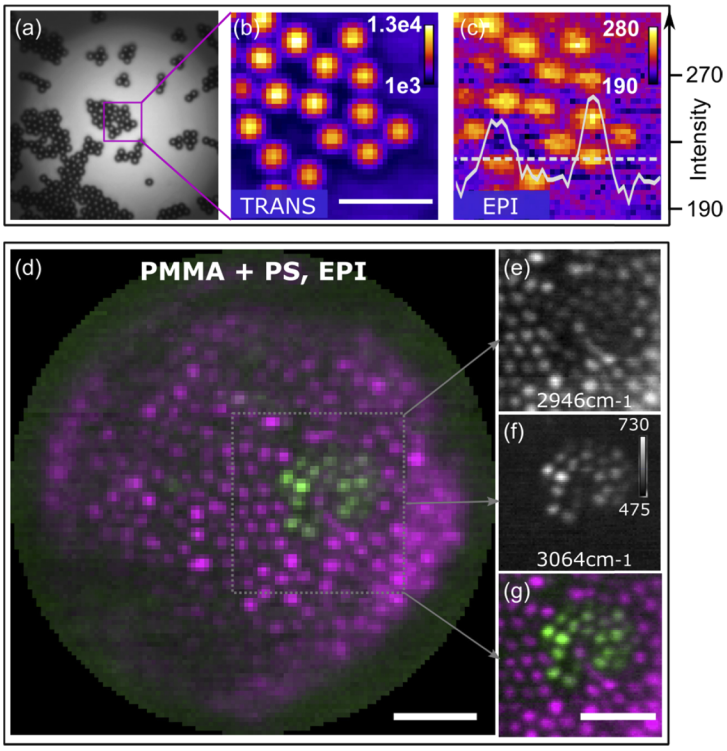

Fig. 3. (a-c): CARS images from a sample with 2 µm diameter PS beads. (a): bright-field image of the sample area. (b, c): CARS signal detected in (b) transmission and (c) epi-detection at a Raman resonance of 3060 cm^{-1}. Integration time = 10 ms. Scalebar in (b) is 5 µm. The inset graph in (c) shows the intensity of the signal in (c) along the dashed line. (d-g): CARS images from a sample with both 2.5 µm diameter PMMA beads and 2 µm diameter PS beads, detected in epi-detection at Raman resonance of (e) 2946 cm^{-1} and (f) 3064 cm^{-1}, respectively. (g): overlay of (e) and (f), where green represent the image at 3064 cm^{-1} and magenta the image at 2946 cm^{-1}. (d): overlay of the full field of view. Scalebars in (d), (f) are 10 µm.

Optics EXPRESS

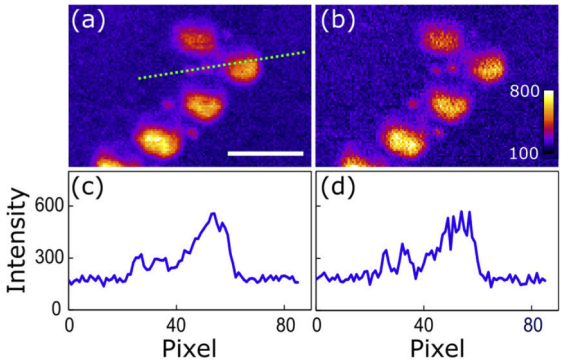

Fig. 4. CARS signal from 2 µm, and 7 µm diameter PS beads, detected in epi-detection using (a) 2 ms and (b) 1 ms integration time at a frequency shift of 3056 cm^{-1}. The noise visible in (b) is mainly due to the SLM. (c,d): The intensity of the signal in (a,b) along the dashed line shown in (a). Interference effects due to the coherent signal and excitation distort the shape of the 7 µm beads. The scalebar is 10 µm.

give an effective NA equal to that of the fibre. The focus at the distal end of the fibre was created by interference of the two polarization paths, and any phase mismatch between them caused a significant drop in the focusing quality. In order to keep the two input polarisation paths in phase, a fraction of the pump and Stokes beams was picked-off using an AR-coated glass plate placed before the microscope objective, at a small angle to the beam. The beams were passed through a polariser at 45 degrees, split on a dichroic mirror (DMLP805T, Thorlabs) and sent to two photodiodes. At the start of every 2 scanlines for dataset 1 and every 10 scanlines for dataset 2, the relative phase of the two polarisation paths was determined using phase stepping interferometry, using the SLM to shift the phase of the signal, and the phase difference was reset to zero by changing the offset phase of the patterns on the SLM.

The light from the fibre output end was collected using a second 20X NA 0.45 objective lens, and for the calibration step, the plane at which we wanted to create the focused spots (here, located 50 µm from the fibre facet) was imaged onto a camera with a pixel size of 5.86 µm, using a 200 mm achromatic lens. The reference beam was collimated after the iris using a f = 200 mm achromatic lens and was adjusted to have the same path length as the optical path through the fibre. The polarisation of the reference beam was linear, resulting in linearly polarised focused spots in the imaging plane after the calibration. (In effect, via the calibration method, we optimize the signal in the polarization direction set by the reference beam). The light from the fibre was overlapped with the reference beam using a beam splitter cube.

For collecting the signal in transmission the light was sent to a multialkali PMT (Hamamatsu H10723) (dataset 1) or a GaAsP PMT (PMT2101, Thorlabs) (for dataset 2). The signal was filtered using a shortpass filter (Brightline SP650, Semrock) and a bandpass filter (Brightline 550/88, Semrock). For epi-detection the light was collected back through the fibre, reflected of a dichroic mirror (DMLP605, Thorlabs), filtered using a shortpass filter (FESH0600, Thorlabs) and a bandpass filter (Brightline 550/88, Semrock) and detected on a PMT (PMT2101, Thorlabs).

For transparent samples, we focused approximately on the sample using white light sent through the fibre (LED1 in Fig. 1) and the same camera as used for calibration focused onto the imaging plane. For scattering samples and for navigating the sample, we used an LED and a camera imaging the fibre end and sample at a shallow angle from the fibre side of the sample.

The fibre was a GRIN fibre with 50 µm core, 125 µm cladding and 0.29 NA (Prysmian DrakaElite). The fibre coating was stripped and the fibre was cut to 30–35 mm length, cleaved to a flat facet and mounted in a ferrule with low refractive index glue (n = 1.375). Mounting using

Optics EXPRESS

the low refractive index glue allowed collection of the signal through the cladding in addition to through the core.

2.2. Fibre calibration procedure

In the following, we will refer to a point focused on the input facet of the fibre (corresponding to single grating on the SLM) as an "input mode" and a focused spot at a position (x,y) on the output facet as an "output mode".

The usable range of input modes were found by raster scanning a point in a square grid across the input facet of the fibre using consecutive gratings on the SLM. The intensity was summed on the camera for the pixels in the area corresponding to the fibre core. Only the modes that gave at least 20% (for dataset 2) or 50% (for dataset 1) light transmission, relative to the input modes near the center of the fibre, were selected. The SLM patterns corresponding to these modes were then displayed one at a time and the output speckle pattern from the fibre was overlapped with the reference beam on the camera. The phase of the SLM pattern was shifted in 4 steps across a range of 2π, twice, and the intensity for each output mode was recorded. The phase (relative to the reference) as well as the amplitude of each output mode for each input mode was then calculated. A focused spot at a plane behind the output facet of the fibre could then be created by combining all the input modes with a phase set to achieve constructive interference at the chosen output point. For dataset 1 only the phase of the pattern was used, whereas for dataset 2 both amplitude and phase was used. Using the amplitude information ensures that only input modes that contribute to the interference are used and modes that would mainly increase the speckle background are suppressed. All the spots were created 50 µm from the fibre facet.

The calibration was performed once for each beam and input polarisation. During the calibration only one beam at a time was incident on the SLM and the other one was blocked. Thus each calibration step proceeds as for a single wavelength system. The patterns from each calibration run were then simply added on the SLM. More precisely, the hologram displayed on the SLM should have the form of $\arg(\mathrm{IFT}(F_\mathrm{P}))$ for the pump wavelength and $\arg(\mathrm{IFT}(F_\mathrm{S}))$ for the Stokes wavelengths, where F_P and F_S are the fields for the pump and Stokes wavelengths that should be projected on the proximal facet of the fibre in order to create a point at a distal end, IFT stands for the inverse Fourier transform (since the fibre facet was in the Fourier plane of the SLM) and arg is the argument of the complex number (since we used a phase-only SLM). In order to generate F_P and F_S simultaneously we displayed a hologram that had the form $\arg(\mathrm{IFT}(F_\mathrm{P} + F_\mathrm{S}))$. Furthermore, since the CARS signal depends quadratically on the pump intensity, we additionally increased the weight of the gratings for the pump beam, resulting in a hologram described by $\arg(\mathrm{IFT}(2F_\mathrm{P} + F_\mathrm{S}))$. This increased the power in the spot for the pump beam at the cost of a decreased power of the Stokes beam. Both beams interact with both patterns, but the interaction with the wrong wavelength (e.g. the pump beam interacting with the pattern for the Stokes beam) only produced a speckle pattern after the fibre and no focus. In addition, a fraction of that light was incident outside the fibre core, and did not reach the sample. This speckle background is, however, without significant impact for CARS imaging. This since the signal depends on the intensity as $(I_\mathrm{P}{}^2 I_\mathrm{s})$, and the low intensity speckle patterns for the pump and Stokes wavelength are largely uncorrelated. Thus the signal is generated entirely at the focused spot.

The transmission of the setup, defined as (the power in the focused spot)/(the input power to the setup) was 7.5% for the pump beam and 2.5% for the Stokes beam. The lower transmission of the Stokes beam was mainly due to the 2:1 ratio of the grating amplitudes on the SLM, as discussed above. This could be mitigated by using separate parts of the SLM for the different beams, which would also increase the transmission for the pump beam somewhat.

We used 2400 input modes per polarisation for the pump beam and 1600 for the Stokes beam, and about 33000 output modes. The fibre had 1162 modes at the pump wavelength and 750 modes at the Stokes wavelength. For imaging PS and PMMA in the same image, we calibrated the

Optics EXPRESS

fibre at a pump wavelength in between the two resonant wavelengths (the wavelength dependence of the setup is discussed in Sec. 2.3). The complete calibration takes approximately 15 minutes on the Meadowlark HSP1920-1064-HSP8 SLM, but it is useable for a few hours of imaging.

The pixel spacing in the sample plane during imaging is determined by the camera resolution during the calibration. Here we used a pixel spacing of 0.26 µm. During imaging we can set the pixel step to multiples of this value. The FWHM of the created spots near the center of the fibre core was measured to 1.23 and 1.55 µm for the pump and Stokes wavelength, respectively, which was similar to the FWHM expected from the NA of the fibre. The size of the foci increased towards the edges of the fibre facet, as expected for a GRIN fibre.

2.3. Wavelength dependence of the excitation power

The created focus is only optimal at the calibration wavelength. As the Raman pump laser is tuned away from the calibration wavelength to access different Raman shifts, the power in the spot drops. This is mainly due to the dispersion of the SLM pattern [30], which consists of overlayed gratings. The fibre used here had a bandwidth of 75 nm and is thus not a limiting factor [26]. To correct for this, we characterized the spot for the used wavelengths. The power ratio (the quotient of the power in the focused spot and the total transmitted power) and size of the focused spot as a function of OPO wavelength was measured by calibrating the fibre at a wavelength λ_0, and then tuning the wavelength, λ, of the OPO, using the same SLM pattern, while imaging the focused spot. This data is then corrected for the wavelength dependence of the camera response as well as the wavelength dependence of the filters in front of the camera. This information is then used to correct the measured CARS intensity in the wavelength dependent measurements.

2.4. Zemax modelling

To model the collection efficiency of the probe when collecting a signal scattered from tissue in epi-detection, we used non-sequential ray tracing with a Henyey-Greenstein (HG) model in Zemax Optics Studio 17.5. In this model, a laser beam with a wavelength of 660 nm and a power of 1W was focused by an AR coated lens with numerical aperture 0.3 into the specimen volume. The specimen volume was set to non-reflecting with an index of refraction of 1.33, a mean free path of 100 µm and anisotropy factor 0.93. From the ray-tracing, we obtained the back scattered power at a virtual detector placed between the lens and the specimen volume. The back-scattered power for a 125 µm detector aperture (corresponding to collection through both the core and cladding of the fibre) is 17.7 mW, corresponding to a 1.77% collection efficiency. For a smaller detector aperture of 50 µm (the size of the fibre core) the back-scattered power was 4.4 mW.

2.5. Sample preparation

Polystyrene (PS) beads of diameter 2 and 7 µm and PMMA beads of diameter 2.5 µm, (Sigma Aldrich 78452-5ml-F, and 78462-5ML-F, and Bang laboratories PP05N) were deposited on type 1.5 cover slips. For some samples (the data presented in Fig. 4) a scattering layer was deposited on the reverse side of the coverslip to better simulate the detection mechanism in tissue. The scattering layer consisted of 2-3% intralipid solution (Sigma Aldrich I141-100ML) in epoxy, that was left to set overnight. It has been shown that 2–3% intralipid solution corresponds to scattering coefficients similar to (brain) tissue (µs'=20–30 cm^{-1} [27]).

2.6. CARS imaging

The power on the sample in the focused spot was about 7 mW (8.5 mW) for the pump beam and 6 mW (3 mW) for the Stokes beam for dataset 1 (dataset 2) respectively. This corresponds to 0.6 MW/cm^2 (0.7 MW/cm^2) for the pump beam and 0.3 MW/cm^2 (0.2 MW/cm^2) for the Stokes beam for dataset 1 (dataset 2) respectively. The laser pulse durations are 1–2 ps, the bandwidth

Optics EXPRESS

of the pump beam is 13–22 cm^{-1} (depending on the wavelength and the pumping condition of the OPO) and the bandwidth of the Stokes beam is approximately 10 cm^{-1}.

The focus is scanned across the sample using the SLM. The total pixel dwell time consisted of the wait time for the SLM pattern to form completely and the data collection time (integration time). For dataset 1 the integration time was 2 ms and the wait time was 25 ms. For dataset 2, and integration times of 1–2 ms, the wait time was set to 15 ms. For longer integration times of 10 ms and 5 ms, the wait time was reduced to 10 ms. The signal was collected at 165 kHz on a NI DAQ card and averaged over the entire integration time. The bandwidth of the PMT was set to 250 kHz. For the measurements of the wavelength dependence of the CARS signal (Fig. 2), we corrected the data for the wavelength dependence of the laser power and power ratio.

3. Results

We performed CARS imaging through a multimode GRIN fibre using a ps laser and OPO as CARS Stokes and pump excitation sources. The focus, created by shaping the wave-front at the input facet of the multimode fibre, is scanned across a plane situated 50 μm from the output facet of the multimode fibre, mimicking a laser scanning microscope. The total laser power at the sample plane was 11.5–13 mW, and the pulse duration about 1–2 ps.

Figure 2 shows CARS images of (a) 2.5 μm diameter PMMA beads and (b) 2 μm diameter PS beads, deposited on a glass coverslip, as a function of the frequency difference between the pump and Stokes beams, detected in transmission. Figure 2(c) is a plot of the intensity of the signals (averaged over two beads) from Fig. 2(a) and 2(b). This clearly demonstrates that we were able to generate a detectable CARS signal from beads as small as 2 μm, despite the low laser powers and low NA of the fibre (NA = 0.29). Furthermore, we achieved clear chemical contrast allowing us to differentiate between PS and PMMA.

Figures 3(b)–3(c) show CARS images of 2 μm diameter PS beads detected in (b) transmission and (c) epi-detection through the fibre. A bright-field image of the sample area illuminated through the fibre is shown in Fig. 3(a). The inset graph in Fig. 3(c) shows the signal intensity along the dashed line in Fig. 3(c). Figures 3(d)–3(g) show the epi-detected images of a sample with PMMA and PS beads imaged at Raman resonances at 2946 cm^{-1} and 3064 cm^{-1} respectively. Figure 3(g) show an overlay of Figs. 3(e) and 3(f). Figure 3(d) shows the corresponding full field of view. Figure 3 clearly illustrates that epi-detection of the CARS signal is possible, and that the chemical contrast is retained. In epi-detection the signal was nearly 50 times weaker than the signal detected in transmission. This is consistent with that the forward generated signal was being reflected off the glass-air interface of the coverslip (ca 4% reflectivity), and thus directed back towards the fibre. In standard CARS microscopy, the epi-detected signal is the back scattered signal from the tissue or a tissue phantom, and it can reach up to 30% (ref. 23) of the forward generated signal, dependent on the size of the aperture of the collecting objective [24]. For the small aperture size used here (125 μm diameter, since we collected the signal through both the core and the cladding of the fibre), Zemax modelling indicated a collection efficiency of 1–2%, comparable to the reflectivity of the coverslip.

Figures 4(a) and 4(b) show epi-detected CARS images of 2 μm and 7 μm diameter PS beads using 2 ms and 1 ms integration time, respectively. Figures 4(c) and 4(d) show the signal intensities along the dashed line in Fig. 4(a) for the data in Fig. 4(a) and 4(b), respectively. We were able to reduce the integration time to 1 ms, while still imaging 2 μm PS beads with good SNR. In fact, the noise visible in Fig. 4(b) is mainly due to the SLM, which displays changes in the pattern amplitude, resulting in changes of the excitation intensity, at a frequency of approximately 370 Hz. We note that this could be mitigated by a simple noise-eater in the beam path.

Optics EXPRESS

4. Discussion

We have demonstrated CARS microscopy of polymer microspheres through a multimode fibre endoscope. Using an integration time of 1 ms and epi-detection, we imaged 2 μm PS beads with good SNR, indicating sufficient excitation and collection efficiency for a variety of bioimaging applications. Increasing the excitation power would allow shorter integration times. In fact, typical laser intensities in CARS microscopy are several tens of mWs, and at those power levels we would obtain signal levels at least two orders of magnitude higher than demonstrated here. Even though the power transmission of a typical fibre imaging setup likely limits the power at the sample to a few tens of mW for standard laser sources, this would allow integration times of <100 μs. In our setup the power at the sample plane was primarily limited by the onset of sample damage. The SLM takes 10–15 ms to update the hologram and form a new focal spot. During this time period the spot deforms and gradually moves from one focal position to the next. Although no signal was collected during this time, the laser was still exposing the sample over a small area, resulting in damage at higher laser powers. This could be overcome by using a beam-blanking device, thereby only exposing the sample during signal collection. Furthermore, future developments in fibre production would enable manufacturing of GRIN fibres with higher NA, which would substantially increase the signal generation efficiency.

The limiting factor for the achievable frame rate was the SLM, which takes 10–15 ms to form the hologram completely. Higher speeds could be reached by SLM overdriving, potentially reaching about 1 kHz switching rate [28]. Separately, for one-photon fluorescence imaging using a DMD, pixel dwell times as short as of 30 μs have been demonstrated [10]. These devices are, however, lossy and thus not suitable for delivering the high excitation powers needed for nonlinear microscopy. In the future, pure phase modulating micromirror-based devices with acceptable pixel numbers [29] could deliver comparable speed to DMDs combined with an efficiency approaching that of liquid crystal SLMs.

As is well established by previous studies [19,23], CARS offers much higher imaging rates compared to linear Raman scattering (which was previously demonstrated through multimode fibres using pixel dwell times of a few seconds [17,18]) while still providing sufficient specificity to distinguish cell components such as lipids and proteins [16,30], making it much more suitable for applications in clinical practice, even with the moderate refresh rate of the SLM used here.

The signal intensity is not even across the field-of-view, as seen in Fig. 3(d), because the quality of the focus for the two wavelengths varies across the sample plane. This could, however, be corrected for by measuring the intensity and size of the focus across the field-of-view directly after calibration. The excitation power can then be adjusted directly on the SLM during imaging, resulting in an even intensity.

We also note that the methods for calibration and CARS imaging presented here, work regardless of the shape of the fibre, as long as it is static, and for GRIN fibres even small changes in bending can be tolerated [31].

Finally, we note that the background speckle pattern, inherent in imaging through multimode fibres, is almost without significance here. Not only is it suppressed because of the non-linear dependence of the signal on the excitation intensity, but the fact that the signal is generated by the product of two wavelengths with different and uncorrelated speckle patterns, means that the background is negligible. In contrast, in linear imaging techniques (one-photon fluorescence, reflectance, linear Raman imaging, etc.) the speckle pattern results in a reduced image contrast. The uncorrelated nature of the two speckle patterns also reduces problems normally associated with delivery of the excitation pulses through a fibre. The generation of a four-wave mixing (FWM) signal in the fibre is an issue in fibre endoscopes and fibre delivery systems for CARS imaging. However, in most cases where FWM is an issue, a single mode fibre, tens of centimeters long, is employed, resulting in a small mode field diameter (and thus high intensity) and a long interaction length. In general, for a multimode fibre, the light is in the form of a low intensity

Optics EXPRESS

speckle pattern. Even for a GRIN fibre, where the speckles are larger and brighter than for step-index fibres, the power in the brightest speckles is about a factor of 10 lower than the power of the laser, in a speckle the size of a few μm across or more. In addition to this, the overlap between the uncorrelated speckles from the pump and Stokes beams is low, resulting in a very inefficient FWM process. In addition, the total fibre length is only 3 cm. For GRIN fibres, the source of the FWM signal is more likely to be the foci inside the fibre that arise from the self-imaging properties of the fibre. The field in the fibre is periodically repeated every self-imaging distance (~400 μm for the fibre used here) although with gradually decreasing fidelity due to the fibre imperfections. An estimate of the size of these foci is that they have the same size as the focus in the sample plane (~1.5 μm diameter, ~12μm length). Even if we assume that the self-imaging is retained throughout the fibre, which it likely is not, the total interaction length is a mere 0.9 mm. For the 1–2 ps pulses used here, the FWM signal will thus be small, which is in line with that the signal from the beads is clearly detectable above the combined background from the fibre and the sample.

5. Conclusion

In summary, we have demonstrated CARS microscopy through a single multimode fibre, which has the potential to be the least invasive and fastest label-free endoscopic bio-imaging method with chemical contrast reported so far.

This study clearly demonstrates that it is feasible to perform CARS imaging through a multimode fibre with reasonable integration times also for structures as small as 2 μm diameter beads. Further development, primarily adding a beam blanking unit to the system, to allow the use of higher laser powers, should allow us to push the integration time below 100 μs. Future new modulation devices, based on micromirrors should allow matching scan speeds. Successfully demonstrating that CARS imaging is possible despite the small footprint and thus collection area of the fibre, paves the way for other coherent nonlinear imaging techniques like SRS and THG, where the detection relies mainly on back scattered light from the underlying tissue [25]. The technique could also be combined with other non-linear imaging techniques such as SHG and two-photon fluorescence, allowing for example cancer diagnosis in-situ via a minimally invasive probe.

Funding

European Regional Development Fund (CZ. 02.1.01/0.0/0.0/15_003/0000476, CZ.1.05/2.1.00/01.0017); European Research Council (724530); Ministerstvo Školství, Mládeže a Tělovýchovy (LO1212); Akademie Věd České Republiky (RVO:68081731); Thüringer Ministerium für Wirtschaft, Wissenschaft und Digitale Gesellschaft; Thüringer Aufbaubank.

Acknowledgments

Denis Akimov is acknowledged for help with the OPO. Prysmian Group is gratefully acknowledged for the high NA GRIN fiber sample. Petr Jákl is acknowledged for the development of the camera toolbox.

Disclosures

The authors declare no conflicts of interest.

References

1. C. Krafft, M. Schmitt, I. Schie, D. Cialla-May, C. Matthaeus, T. Bocklitz, and J. Popp, "Label-free molecular imaging of biological cells and tissues by linear and non-linear raman spectroscopic approaches," Angew. Chem., Int. Ed. **56**(16), 4392–4430 (2017).

Optics EXPRESS

2. C. Krafft, I. Schie, T. Meyer, M. Schmitt, and J. Popp, "Developments in spontaneous and coherent raman scattering microscopic imaging for biomedical applications," Chem. Soc. Rev. **45**(7), 1819–1849 (2016).
3. A. Lombardini, V. Mytskaniuk, S. Sivankutty, E. R. Andresen, X. Chen, J. Wenger, M. Fabert, N. Joly, F. Louradour, A. Kudlinski, and H. Rigneault, "High-resolution multimodal flexible coherent raman endoscope," Light: Sci. Appl. **7**(1), 10 (2018).
4. A. Lukic, S. Dochow, H. Bae, G. Matz, I. Latka, B. Messerschmidt, M. Schmitt, and J. Popp, "Endoscopic fiber probe for nonlinear spectroscopic imaging," Optica **4**(5), 496–501 (2017).
5. I. M. Vellekoop and A. P. Mosk, "Focusing coherent light through opaque strongly scattering media," Opt. Lett. **32**(16), 2309–2311 (2007).
6. S. Rotter and S. Gigan, "Light fields in complex media: Mesoscopic scattering meets wave control," Rev. Mod. Phys. **89**(1), 015005 (2017).
7. T. Čižmár and K. Dholakia, "Shaping the light transmission through a multimode optical fibre: complex transformation analysis and applications in biophotonics," Opt. Express **19**(20), 18871–18884 (2011).
8. I. T. Leite, S. Turtaev, X. Jiang, M. Šiler, A. Cuschieri, P. S. J. Russell, and T. Čižmár, "Three-dimensional holographic optical manipulation through a high-numerical-aperture soft-glass multimode fibre," Nat. Photonics **12**(1), 33–39 (2018).
9. T. Nemoto, R. Kawakami, T. Hibi, K. Iijima, and K. Otomo, "Two-photon excitation fluorescence microscopy and its application in functional connectomics," Microscopy **64**(1), 9–15 (2015).
10. S. Turtaev, I. T. Leite, T. Altwegg-Boussac, J. M. P. Pakan, N. L. Rochefort, and T. Čízmár, "High-fidelity multimode fibre-based endoscopy for deep brain in vivo imaging," Light: Sci. Appl. **7**(1), 92 (2018).
11. S. A. Vasquez-Lopez, R. Turcotte, V. Koren, M. Plöschner, Z. Padamsey, M. J. Booth, T. Čižmár, and N. J. Emptage, "Subcellular spatial resolution achieved for deep-brain imaging in vivo using a minimally invasive multimode fiber," Light: Sci. Appl. **7**(1), 1–6 (2018).
12. M. Plöschner, V. Kollárová, Z. Dostál, J. Nylk, T. Barton-Owen, D. E. K. Ferrier, R. Chmelík, K. Dholakia, and T. Čižmár, "Multimode fibre: Light-sheet microscopy at the tip of a needle," Sci. Rep. **5**(1), 18050 (2015).
13. E. E. Morales-Delgado, D. Psaltis, and C. Moser, "Two-photon imaging through a multimode fiber," Opt. Express **23**(25), 32158–32170 (2015).
14. S. Sivankutty, E. R. Andresen, R. Cossart, G. Bouwmans, S. Monneret, and H. Rigneault, "Ultra-thin rigid endoscope: two-photon imaging through a graded-index multi-mode fiber," Opt. Express **24**(2), 825–841 (2016).
15. E. Kakkava, M. Romito, D. B. Conkey, D. Loterie, K. M. Stankovic, C. Moser, and D. Psaltis, "Selective femtosecond laser ablation via two-photon fluorescence imaging through a multimode fiber," Biomed. Opt. Express **10**(2), 423–433 (2019).
16. F. Lu, S. Basu, V. Igras, M. P. Hoang, M. Ji, D. Fu, G. Holtom, V. A. Neel, C. W. Freudiger, D. Fisher, and X. S. Xie, "Label-free dna imaging in vivo with stimulated raman scattering microscopy," Proc. Natl. Acad. Sci. U. S. A. **112**(37), 11624–11629 (2015).
17. I. Gusachenko, M. Chen, and K. Dholakia, "Raman imaging through a single multimode fibre," Opt. Express **25**(12), 13782–13798 (2017).
18. S. Deng, D. Loterie, G. Konstantinou, D. Psaltis, and C. Moser, "Raman imaging through multimode sapphire fiber," Opt. Express **27**(2), 1090–1098 (2019).
19. I. I. Patel, C. Steuwe, S. Reichelt, and S. Mahajan, "Coherent anti-stokes raman scattering for labelfree biomedical imaging," J. Opt. **15**(9), 094006 (2013).
20. H. Wang, Y. Fu, P. Zickmund, R. Shi, and J.-X. Cheng, "Coherent anti-stokes raman scattering imaging of axonal myelin in live spinal tissues," Biophys. J. **89**(1), 581–591 (2005).
21. M. Welte, "As the fat flies: The dynamic lipid droplets of drosophila embryos," Biochim. Biophys. Acta **1851**(9), 1156–1185 (2015).
22. C. D. Napoli, I. Pope, F. Masia, W. Langbein, P. Watson, and P. Borri, "Quantitative spatiotemporal chemical profiling of individual lipid droplets by hyperspectral cars microscopy in living human adipose-derived stem cells," Anal. Chem. **88**(7), 3677–3685 (2016).
23. C. L. Evans, E. O. Potma, M. Puorishaag, D. Côté, C. P. Lin, and X. S. Xie, "Chemical imaging of tissue in vivo with video-rate coherent anti-stokes raman scattering microscopy," Proc. Natl. Acad. Sci. U. S. A. **102**(46), 16807–16812 (2005).
24. B. G. Saar, C. W. Freudiger, J. Reichman, C. M. Stanley, G. R. Holtom, and X. S. Xie, "Video-rate molecular imaging in vivo with stimulated raman scattering," Science **330**(6009), 1368–1370 (2010).
25. D. Débarre, N. Olivier, and E. Beaurepaire, "Signal epidetection in third-harmonic generation microscopy of turbid media," Opt. Express **15**(14), 8913–8924 (2007).
26. T. Pikálek, J. Trägårdh, S. Simpson, and T. Čižmár, "Wavelength dependent characterization of a multimode fibre endoscope," Opt. Express **27**(20), 28239–28253 (2019).
27. M. Johns, C. A. Giller, D. C. German, and H. Liu, "Determination of reduced scattering coefficient of biological tissue from a needle-like probe," Opt. Express **13**(13), 4828–4842 (2005).
28. G. Thalhammer, R. W. Bowman, G. D. Love, M. J. Padgett, and M. Ritsch-Marte, "Speeding up liquid crystal slms using overdrive with phase change reduction," Opt. Express **21**(2), 1779–1797 (2013).
29. T. A. Bartlett, W. C. McDonald, and J. N. Hall, "Adapting Texas Instruments DLP technology to demonstrate a phase spatial light modulator," Proc. SPIE **XI**, 27 (2019).

Optics EXPRESS

30. T. Meyer, M. Chemnitz, M. Baumgartl, T. Gottschall, T. Pascher, C. Matthaus, B. F. M. Romeike, B. R. Brehm, J. Limpert, A. Tunnermann, M. Schmitt, B. Dietzek, and J. Popp, "Expanding multimodal microscopy by high spectral resolution coherent anti-stokes raman scattering imaging for clinical disease diagnostics," Anal. Chem. **85**(14), 6703–6715 (2013).
31. D. E. Boonzajer-Flaes, J. Stopka, S. Turtaev, J. F. de Boer, T. Tyc, and T. Cižmár, "Robustness of Light-Transport Processes to Bending Deformations in Graded-Index Multimode Waveguides," Phys. Rev. Lett. **120**(23), 233901 (2018).